mater.scichina.com link.springer.com

Published online 19 August 2021 | https://doi.org/10.1007/s40843-021-1740-7
*Sci China Mater* 2022, 65(1): 95–104

# Modulating composite polymer electrolyte by lithium closo-borohydride achieves highly stable solid-state battery at 25°C

Kepan Bao[1], Yuepeng Pang[1*], Junhe Yang[1], Dalin Sun[2], Fang Fang[2*] and Shiyou Zheng[1*]

**ABSTRACT** **Rational composite design is highly important for the development of high-performance composite polymer electrolytes (CPEs) for solid-state lithium (Li) metal batteries. In this work, Li closo-borohydride, $Li_2B_{12}H_{12}$, is introduced to poly(vinylidene fluoride)-Li-bis-(trifluoromethanesulfonyl) imide (PVDF-LiTFSI) with a bound *N*-methyl pyrrolidone plasticizer to form a novel CPE. This CPE shows superb $Li^+$ conduction properties, as evidenced by its conductivity of 1.43 × $10^{-4}$ S $cm^{-1}$ and $Li^+$ transference number of 0.34 at 25°C. Density functional theory calculations reveal that $Li_2B_{12}H_{12}$, which features electron-deficient multicenter bonds, can facilitate the dissociation of LiTFSI and enhance the immobilization of TFSI to improve the $Li^+$ conduction properties of the CPE. Moreover, the fabricated CPE exhibits excellent electrochemical, thermal, and mechanical stability. The addition of $Li_2B_{12}H_{12}$ can help form a protective layer at the anode/electrolyte interface, thereby preventing unwanted reactions. The above benefits of the fabricated CPE contribute to the high compatibility of the electrode. Symmetric Li cells can be stably cycled at 0.2 mA $cm^{-2}$ for over 1200 h, and Li||$LiFePO_4$ cells can deliver a reversible specific capacity of 140 mA h $g^{-1}$ after 200 cycles at 1 C at 25°C with a capacity retention of 98%.**

**Keywords:** lithium closo-borohydride, composite polymer electrolytes, lithium dendrite, solid-state lithium batteries

## INTRODUCTION

Solid-state lithium batteries (SSLBs) have attracted considerable attention owing to their potential to mitigate safety issues associated with organic liquid electrolytes, such as leakage, flammability, and short circuiting (*via* dendritic growth) of the batteries [1–4]. Solid electrolytes play a crucial role in the overall electrochemical performance of SSLBs. Polymer electrolytes including poly(ethylene oxide) (PEO) [5,6], poly(acrylonitrile) [7], poly(methyl methacrylate) [8], and poly(vinylidene fluoride) (PVDF) [9], combined with Li salts such as $LiClO_4$ and Li bis-(trifluoromethanesulfonyl)imide (LiTFSI)), are among the most promising types of solid electrolytes that are currently available because their excellent flexibility and processability render industrial production feasible [10–12].

Extensive efforts have been exerted to optimize the performance of solid polymer electrolytes. One successful strategy involves the incorporation of polymer electrolytes with inert inorganic fillers, such as $TiO_2$ [13], $Al_2O_3$ [14], and $SiO_2$ [15]. This approach can achieve the following: (i) generate rapid $Li^+$ transfer channels by forming a local amorphous region, (ii) free $Li^+$ and immobilize the anion of Li salts *via* atomic interactions, and (iii) enhance the mechanical properties of the resultant material owing to the adhesion effect with polymers. Inorganic $Li^+$ conductors, such as $Li_{0.3}La_{0.7}TiO_3$ [16], $Li_7La_3Zr_2O_{12}$ (LLZO) [17], $Li_{1.3}Al_{0.3}Ti_{1.7}(PO_4)_3$ (LATP) [18], $Li_{1+x}Al_xGe_{2-x}(PO_4)_3$ [19], and $Li_{10}GeP_2S_{12}$ (LGPS) [19], can effectively improve the $Li^+$ conduction properties of composite polymer electrolytes (CPEs) as active fillers. In-depth investigations have revealed that active fillers can provide additional $Li^+$ transfer pathways in CPEs and elevate the $Li^+$ concentration in the space-charge region at the filler/polymer interface [20]. For example, Zhang *et al.* [21] reported that LLZO could significantly improve the $Li^+$ conductivity of PVDF-$LiClO_4$ by triggering structural modifications *via* the interactions among LLZO, PVDF, and $LiClO_4$. Yang *et al.* [22] prepared a CPE composed of LATP, PEO-LiTFSI, and a 2D planar oligomer. In this work, LATP served as a physical barrier against Li dendrites and provided rapid transfer pathways for $Li^+$, while the 2D planar oligomer enhanced contact with the electrodes. Pan *et al.* [23] prepared a flexible CPE of LGPS/PEO-polyethylene glycol-LiTFSI by introducing a bridge builder (i.e., a silane coupling agent); the resultant materials exhibited rapid $Li^+$ transfer and a high $Li^+$ transference number arising from the strong chemical bonds in the CPE.

Although the above pioneering studies have made great contributions to the development of CPEs, further improvement, especially in terms of $Li^+$ conduction properties and electrode compatibility, remains necessary to expand the practical applications of these materials. The design of novel compositions is a promising approach for developing advanced CPEs. Li borohydrides have recently drawn increased attention as solid electrolytes on account of their superior $Li^+$ conducting properties [24] and Li metal compatibility [25–28]. For example, $Li_2B_{12}H_{12}$ [29] exhibits high $Li^+$ conductivity (2.60 × $10^{-4}$ S $cm^{-1}$) and critical current density for Li dendrite formation (2.0 mA $cm^{-2}$) at 75°C [30]. More importantly, because the unique multicenter bonds of $B_{12}H_{12}^{2-}$ present an electron-deficient nature, this component may be expected to interact strongly with Li-salt and increase the $Li^+$ conductivity and transference number of the reaction system. Therefore, we believe that Li borohydrides, especially $Li_2B_{12}H_{12}$, may be promising active fillers for CPEs [31,32].

In this work, $Li_2B_{12}H_{12}$ is introduced to PVDF-LiTFSI due to their high mutual stability. The $Li_2B_{12}H_{12}$/PVDF-LiTFSI CPE

[1] School of Materials Science and Engineering, University of Shanghai for Science and Technology, Shanghai 200093, China
[2] Department of Materials Science, Fudan University, Shanghai 200433, China
[*] Corresponding authors (emails: syzheng@usst.edu.cn (Zheng S); f_fang@fudan.edu.cn (Fang F); pangyp@usst.edu.cn (Pang Y))

  

(LBH-CPE) shows superior $Li^+$ conduction properties and excellent electrochemical, thermal, and mechanical stability, all of which contribute to the stable cycling of symmetric Li and Li||$LiFePO_4$ cells at 25°C. Density functional theory (DFT) calculations reveal that the interaction between $Li_2B_{12}H_{12}$ and LiTFSI is the main contributor to improving the $Li^+$ conduction of LBH-CPE. Moreover, the addition of $Li_2B_{12}H_{12}$ leads to the formation of protective interphase, which is very helpful for improving anode compatibility.

## EXPERIMENTAL SECTION

### Fabrication of the CPEs

LiTFSI (99.95%) and PVDF powders ($M_w$ = 530,000) were obtained from Sigma-Aldrich. *N*-Methyl pyrrolidone (NMP) was purchased from Aladdin. PVDF (0.5 g) and LiTFSI (0.3 g) were dispersed into 5 mL of NMP and magnetically stirred until complete dissolution to obtain a homogeneous solution. Then, $Li_2B_{12}H_{12}$ was added to the solution at weight fractions of 0.5, 1, and 2 wt%. The solutions were sonicated for 1 h, magnetically stirred for 10 h, cast onto glass molds, and dried directly under vacuum at 60°C for 24 h. For comparison, PVDF-LiTFSI was fabricated under the same conditions but without the addition of $Li_2B_{12}H_{12}$.

### Structural characterization

Scanning electron microscopy (SEM) images were obtained with the Quanta FEG 450 instrument (FEI, USA). X-ray diffraction (XRD) patterns were characterized by an Ultima IV instrument (Rigaku, Japan) with a scan rate of 5° $min^{-1}$. Fourier transform infrared (FTIR) spectra were acquired from a Nicolet iS5 system (Thermo Scientific, USA). Thermogravimetric analysis (TGA) was performed with a Discovery TGA5500 system (TA, USA) under a $N_2$ atmosphere and a heating rate of 10°C $min^{-1}$. Stress-strain curves were obtained by a CMT6103 universal testing machine (MTS, USA).

### Electrochemical measurements

The fabricated materials were assembled into a CR2032-type cell. Steel foil, Li foil, and $LiFePO_4$-based composite pellets ($LiFePO_4$:C:PVDF = 8:1:1 on Al foil) were used as electrodes. Electrochemical impedance spectroscopy (EIS) and direct current (DC) polarization were performed using an Interface 1000E system (Gamry, USA). The DC polarization voltages were set to 1 V for the electronic transference number tests and 10 mV for the $Li^+$ transference number tests. Linear sweep voltammetry (LSV) curves were obtained using a CHI660E workstation (Chenhua, China) with a scan rate of 10 mV $s^{-1}$. Galvanostatic charge/discharge (GCD) measurements were performed using a CT2001A test system (Land, China).

### First-principles calculations

All first-principles calculations conducted in this work were performed using the Vienna *Ab initio* Simulation Package [33]. The plane-wave basis set method based on DFT was adopted with ultra-soft pseudopotentials [34] and Perdew-Burke-Ernzerhof (PBE) parameterization [35,36] of the generalized gradient approximation. vdW-D3 was invoked as a non-local correlation functional in all calculations to account for dispersion interactions between different ions and substrates [37]. An energy cutoff of 500 eV was used for the plane-wave basis set, and a 1 × 1 × 1 Monkhorst-Pack mesh grid for sampling *k* points was established for the Brillouin zone integration of the different systems. These settings were verified by obtaining a total energy convergence of less than 1 meV $atom^{-1}$. Geometry relaxation was conducted prior to examining the structural properties and total energies, and it revealed that the force on each atom converged below a threshold of 0.01 eV $Å^{-1}$.

## RESULTS AND DISCUSSION

Fig. 1a schematically illustrates the preparation procedure and composition design of LBH-CPEs. Our design is expected to promote rapid $Li^+$ conduction, considering the unique interactions among the material components. Optical photographs of PVDF-LiTFSI and LBH-CPEs with different $Li_2B_{12}H_{12}$ contents are displayed in Fig. 1b. PVDF-LiTFSI without $Li_2B_{12}H_{12}$ is white and transparent. When $Li_2B_{12}H_{12}$ is introduced to the reaction system, the LBH-CPEs turn yellow, and the intensity of their color increases with increasing $Li_2B_{12}H_{12}$ content. The optical photograph (Fig. 1c) of bent LBH-CPE shows that this film is highly flexible. Fig. 1d, e present the top-view and cross-sectional SEM images of 1 wt% LBH CPE (1LBH-CPE). A smooth surface with few pores can be observed in the top-view SEM image, which is a typical morphology of tape-casting films (Fig. S1).

$Li_2B_{12}H_{12}$ particles are not found on the surface of the CPE because they are buried in the PVDF-LiTFSI matrix. In the cross-sectional image, $Li_2B_{12}H_{12}$ particles with diameters of 2–10 μm are implanted in the PVDF-LiTFSI matrix, and the thickness of the LBH-CPE is 130 μm.

Fig. 1f shows the XRD patterns of LBH-CPE and the reference samples (i.e., $Li_2B_{12}H_{12}$, PVDF, and PVDF-LiTFSI). $Li_2B_{12}H_{12}$ exhibits typical diffraction peaks at 15.3° and 17.7° without impurity signals. The XRD pattern of PVDF reveals a strong peak and a shoulder peak at 20.8° and 19.2°, respectively, which correspond to the (110) and (020) planes [38]. After the addition of LiTFSI, no peak was observed that could be attributed to LiTFSI and the peaks of PVDF weakened, thereby indicating the complete dissolution of LiTFSI in PVDF and a significant reduction in PVDF crystallinity. The XRD profile of LBH-CPE only shows weak PVDF peaks, which suggests that the addition of $Li_2B_{12}H_{12}$ can reduce the crystallinity of PVDF further. No signal for $Li_2B_{12}H_{12}$ is visible because of its low content (1 wt%). FTIR measurements (Fig. 1g) were then performed to identify the compositions of LBH-CPE and the reference samples. Typical absorbance bands can be detected for $Li_2B_{12}H_{12}$ and PVDF. The additional bands noted in the FTIR spectrum of PVDF-LiTFSI correspond to LiTFSI and residual NMP. After addition of $Li_2B_{12}H_{12}$, a weak but clear absorbance signal at 2480 $cm^{-1}$ appears (inset, Fig. 1g), thus indicating the existence of $Li_2B_{12}H_{12}$ in LBH-CPE [39]. The above results confirm that no chemical reaction occurs between $Li_2B_{12}H_{12}$, PVDF, LiTFSI, and NMP during the preparation of the CPE (Fig. S2).

The $Li^+$ conduction properties of PVDF-LiTFSI and LBH-CPEs with different $Li_2B_{12}H_{12}$ contents were investigated. Fig. 2a shows the EIS of PVDF-LiTFSI and LBH-CPE-based blocking cells measured at 25°C; semicircles at high frequencies and linear tails at low frequencies can be found in the plots. The chord length of the semicircle corresponds to the resistance of the electrolyte according to the equivalent circuit. Between the two samples, 1LBH-CPE exhibits a lower resistance of 120 Ω, whereas PVDF-LiTFSI reveals a resistance of 700 Ω.

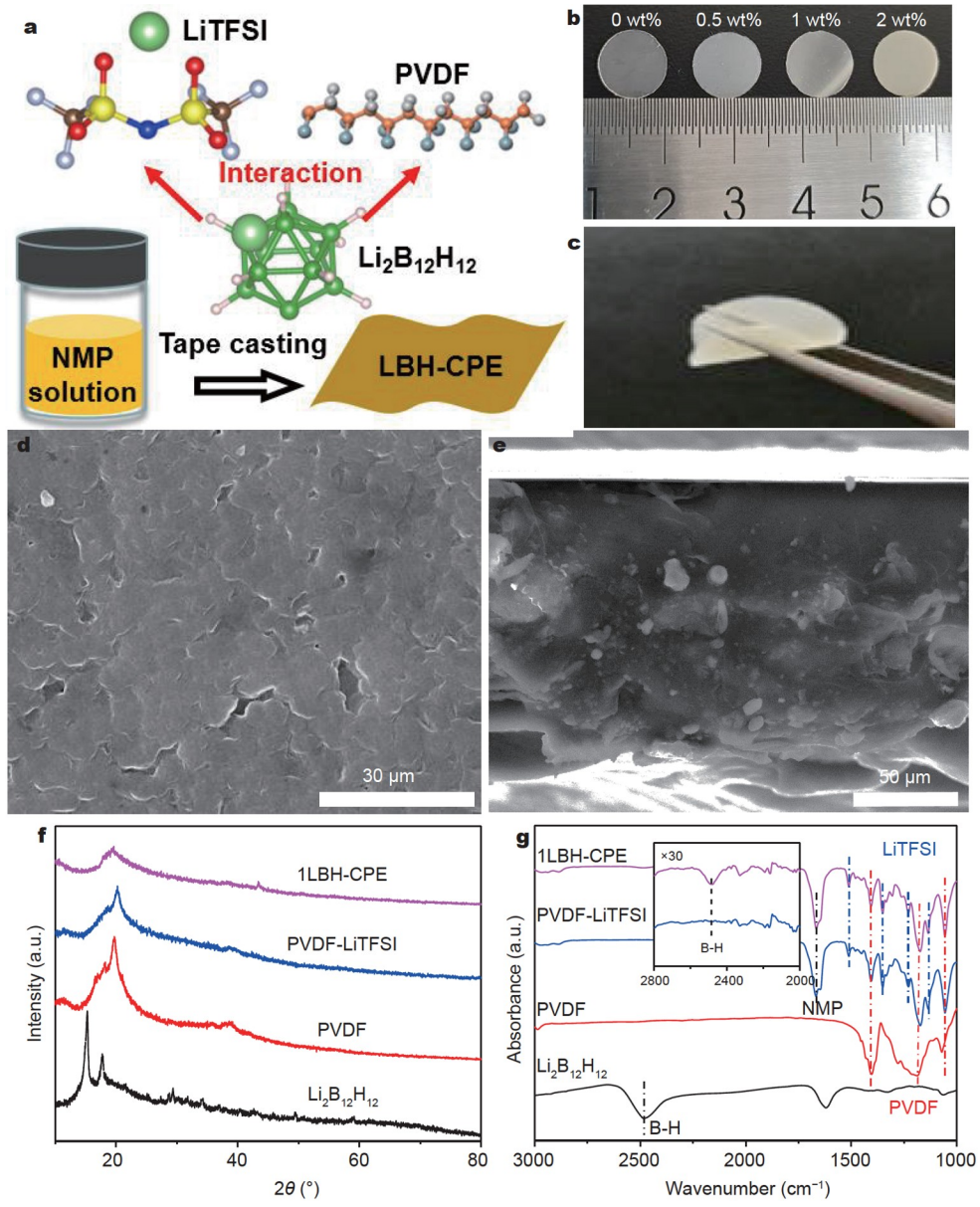


**Figure 1** (a) Schematic illustration of the design principle of LBH-CPEs. (b) Optical photographs of the PVDF-LiTFSI membranes with 0, 0.5, 1 and 2 wt% $Li_2B_{12}H_{12}$. (c) Optical photograph of bent 1LBH-CPE showing good flexibility. (d) Top-view and (e) cross-sectional SEM images of 1LBH-CPE. (f) XRD patterns and (g) FTIR spectra of $Li_2B_{12}H_{12}$, PVDF, PVDF-LiTFSI, and 1LBH-CPE.

The conductivity ($\sigma$) of these materials can be calculated according to the equation:

$$\sigma = \frac{d}{A \times R}, \quad (1)$$

where $d$ is the film thickness, $A$ is the contact area, and $R$ is the film resistance. The temperature-dependent $\sigma$ values of PVDF-LiTFSI and LBH-CPEs are shown in Fig. 2b. Among the samples tested, 1LBH-CPE shows the highest $\sigma$ value, $1.43 \times 10^{-4}$ S cm$^{-1}$ at 25°C and $1.22 \times 10^{-3}$ S cm$^{-1}$ at 95°C. Adding 0.5 and 2 wt% $Li_2B_{12}H_{12}$ to PVDF-LiTFSI increases the $\sigma$ of the material from $2.46 \times 10^{-5}$ to $8.05 \times 10^{-5}$ and to $4.93 \times 10^{-5}$ S cm$^{-1}$, at 25°C, respectively, but these $\sigma$ values are lower than that of the 1 wt% $Li_2B_{12}H_{12}$-added sample. This phenomenon suggests that the percolation threshold of LBH-CPE is only 1 wt% and that increases in $Li_2B_{12}H_{12}$ content may lead to particle agglomeration and surface degradation [40–42]. The formation of rapid $Li^+$ transfer pathways at the interface between $Li_2B_{12}H_{12}$ and PVDF-LiTFSI may be responsible for the $\sigma$ improvement observed in the tested samples.

Fig. 2c illustrates the DC polarization curves of PVDF-LiTFSI and 1LBH-CPE-based blocking cells at 25°C. The steady-state currents were derived from the electron conductivity for PVDF-LiTFSI and 1LBH-CPE, which were calculated to be $6.13 \times 10^{-9}$ and $8.28 \times 10^{-9}$ S cm$^{-1}$, respectively. These values are suitably low for SSLBs. The $Li^+$ transference numbers of PVDF-LiTFSI (Fig. S3) and 1LBH-CPE were determined using DC polarization and EIS measurements on symmetrical Li cells (Fig. 2d). The calculation of $Li^+$ transference number ($T_{Li^+}$) was based on the following equation [43,44]:

  

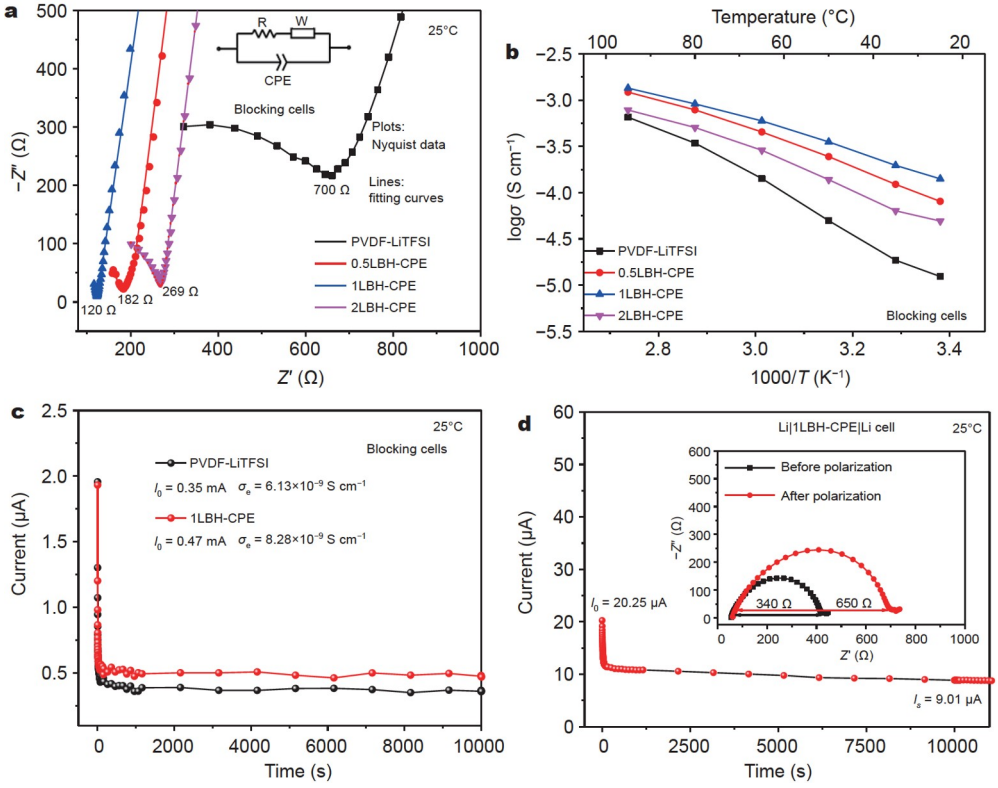


**Figure 2** (a) EIS profiles of PVDF-LiTFSI and CPEs with 0.5, 1, and 2 wt% $Li_2B_{12}H_{12}$ at 25°C. (b) Ionic conductivities of PVDF-LiTFSI and CPEs with 0.5, 1, and 2 wt% $Li_2B_{12}H_{12}$ at different temperatures. (c) Electronic conductivities of PVDF-LiTFSI and 1LBH-CPE. (d) $Li^+$ transference number measurement of 1LBH-CPE.

$$T_{Li^+} = \frac{R_s(\Delta V - I_0 R_0)}{R_0(\Delta V - I_s R_s)}, \quad (2)$$

where $R_s$ and $R_0$ are the interfacial resistances acquired from the diameters of the second semicircles in EIS before and after polarization, respectively; $I_0$ is the initial current; $I_s$ is the steady-state current; and $\Delta V$ is the applied voltage. The calculated $Li^+$ transference number of 1LBH-CPE, at 0.34, is nearly two times that of PVDF-LiTFSI (0.19). The ability of the added $Li_2B_{12}H_{12}$ to remarkably enhance the $Li^+$ transference number may be explained from two perspectives. First, $Li_2B_{12}H_{12}$ is a single $Li^+$ conductor that provides additional transfer pathways for $Li^+$, thus increasing the $Li^+$ transference number [45,46]. Second, the $B_{12}H_{12}^{2-}$ anion possesses electron-deficient multicenter bonds that can immobilize $TFSI^-$ through charge exchange.

DFT calculations were performed to verify the interaction between $Li_2B_{12}H_{12}$ and LiTFSI. The most stable structures of a single LiTFSI molecule and an adsorbed LiTFSI molecule on the $Li_2B_{12}H_{12}$ surface are optimized, as shown in Fig. 3a, b. The $B_{12}H_{12}^{2-}$-terminated (100) surface is an energetically stable adsorption surface. The binding energies of $Li^+$ with isolated $TFSI^-$ and in adsorbed LiTFSI onto the $Li_2B_{12}H_{12}$ (100) surface, as well as the energies between adsorbed $TFSI^-$ and the $Li_2B_{12}H_{12}$ (100) surface are calculated according to the following equation:

$$E_{binding} = E_{total} - (E_A + E_B), \quad (3)$$

where $E_{total}$ is the total energy of the total system, $E_A$ is the energy of a substance A, $E_B$ is the energy of a substance B, and $E_{binding}$ is the binding energy of A with B.

As seen in Table 1, the binding energy between $Li^+$ and $TFSI^-$ is calculated to be −5.18 eV in LiTFSI adsorbed on the $Li_2B_{12}H_{12}$ (100) surface; this value is much lower than that in isolated LiTFSI (−5.93 eV). This result indicates that LiTFSI can be dissociated by the addition of $Li_2B_{12}H_{12}$, which leads to a significant increase in the free $Li^+$ concentration in the reaction system [47,48]. Moreover, the binding energy between $TFSI^-$ and the $Li_2B_{12}H_{12}$ (100) surface was calculated to be −0.89 eV, indicating strong adsorption. The effect of the $Li_2B_{12}H_{12}$ (100) surface on the differential charge density of LiTFSI is displayed in Fig. 3c, d, to illustrate the interaction between $Li_2B_{12}H_{12}$ and LiTFSI further. From these results, we find that the charge depletion region (blue) around Li shrinks when LiTFSI is adsorbed onto the $Li_2B_{12}H_{12}$ (100) surface, which suggests a weakening of the Coulombic force between $Li^+$ and $TFSI^-$. A second finding is that charge exchange occurs between $Li_2B_{12}H_{12}$ and $TFSI^-$, indicating a relatively strong adsorption force between $TFSI^-$ and the $Li_2B_{12}H_{12}$ (100) surface; this finding agrees well with the calculated binding energy between $TFSI^-$ and $Li_2B_{12}H_{12}$. These results reveal that $Li_2B_{12}H_{12}$, which features unique electron-deficient multicenter bonds, can facilitate the dissociation of LiTFSI to provide more free $Li^+$ and enhance the immobilization of $TFSI^-$ by charge exchange. These benefits are mainly responsible for the remarkable improvement in $Li^+$ conduction properties observed in the studied system.

The electrochemical, thermal, and mechanical stabilities of 1LBH-CPE were examined. The electrochemical stability windows of PVDF-LiTFSI and 1LBH-CPE were obtained by the LSV method. Fig. 4a presents the LSV curves of PVDF-LiTFSI and 1LBH-CPE in Li|electrolyte|steel cells at 25°C. After introducing $Li_2B_{12}H_{12}$, the upper limit of the electrochemical stability win-

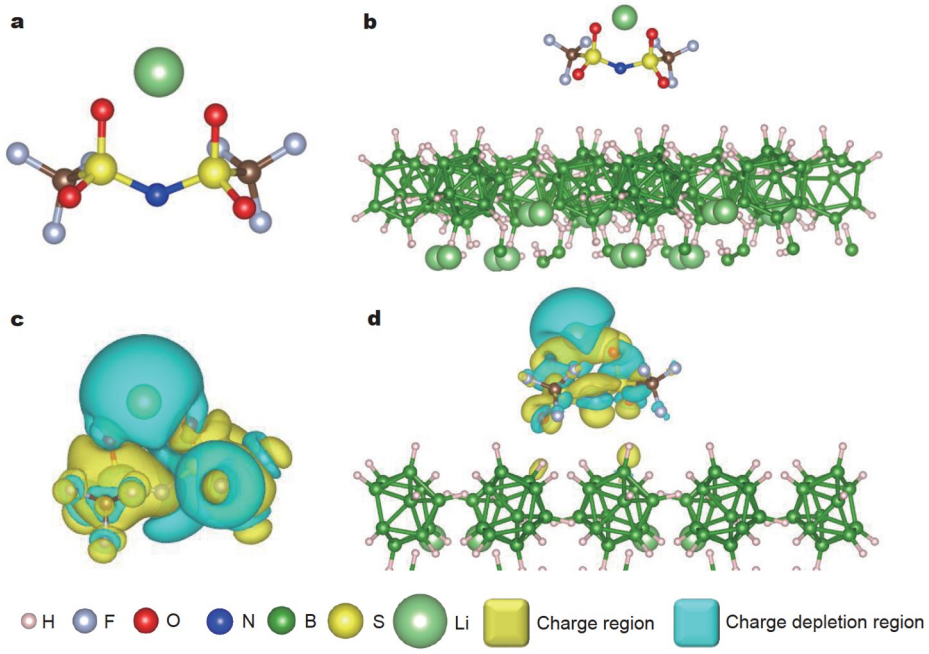


**Figure 3** (a) Molecular structure of LiTFSI. (b) Adsorption of LiTFSI on the $Li_2B_{12}H_{12}$ (100) surface. Computed charge density difference of (c) LiTFSI and (d) LiTFSI adsorbed on the $Li_2B_{12}H_{12}$ (100) surface.

**Table 1** Binding energies between $Li^+$ and $TFSI^-$, $Li^+$ and $TFSI^-$ on $Li_2B_{12}H_{12}$, and $TFSI^-$ and $Li_2B_{12}H_{12}$ obtained by DFT calculations

| Bonds | $E_{total}$ (eV) | $E_A$ (eV) | $E_B$ (eV) | $E_{binding}$ (eV) |
|---|---|---|---|---|
| $[Li^+]_A$ + $[TFSI^-]_B$ | −87.99 | −0.29 | −81.77 | −5.93 |
| $[Li^+]_A$ + $[TFSI^-$ on $Li_2B_{12}H_{12}]_B$ | −1241.42 | −0.29 | −1235.94 | −5.18 |
| $[TFSI^-]_A$ + $[Li_2B_{12}H_{12}]_B$ | −1235.94 | −81.77 | −1153.35 | −0.89 |

dow remains nearly unchanged, as apparent oxidation currents can be observed at >4.0 V for both PVDF-LiTFSI and 1LBH-CPE. Repeated LSV curves obtained over the scanning range of open circuit voltage (OCV) to 0 V are presented in Fig. 4b, which were used to evaluate the electrochemical stability of 1LBH-CPE at low potentials. In the first scan, the reduction current can be detected at <1.5 V and the maximum current reaches 71.0 μA.

In addition, the maximum current decreases to 15.0 and 10.6 μA in the second and third LSV curves, respectively, which indicates the formation of a solid electrolyte interphase (SEI) during scanning. This interphase may help protect the electrolyte from further decomposition. The maximum currents in the first and third OCV-to-0 V scans for PVDF-LiTFSI are 26.0 and 17.0 μA, respectively (Fig. S4). A lower current in the first scan suggests insufficient SEI formation, and a higher current in the third scan suggests poor SEI protection [49]. The above results may be attributed to the formation of a highly protective and conductive LiH-containing SEI through the partial lithiation of added $Li_2B_{12}H_{12}$ (Fig. S5).

The thermal stability of the materials is represented by the TGA curves in Fig. 4c. PVDF exhibits no weight loss until 400°C, which indicates its typical decomposition behavior. In addition, no appreciable weight loss of PVDF-LiTFSI and 1LBH-CPE can be observed at temperatures below 100°C, which confirms that these electrolytes are stable below 100°C. A slow weight loss of 23 wt% can be detected in the temperature range of 100–300°C (Fig. S6), which corresponds to the gradual desorption of residual NMP bound to PVDF-LiTFSI (Figs S7 and S8). The residual NMP mainly acts as a plasticizer to enhance the chain mobility of PVDF, which benefits the $Li^+$ conductivity of the system (Fig. S9). Although this phenomenon remains unclear [50,51], we postulate that this type of CPE is a solid electrolyte, not a gel (Fig. S10). Sharp and slow weight losses successively occur above 300°C, and these weight losses correspond to the decomposition of PVDF and LiTFSI. The addition of $Li_2B_{12}H_{12}$ reduces the decomposition temperatures of PVDF and LiTFSI because of an increase in the amorphous fraction of PVDF and enhancement of the dissociation/immobilization of LiTFSI.

Fig. 4d displays the stress-strain curves of PVDF-LiTFSI and 1LBH-CPE. The introduction of $Li_2B_{12}H_{12}$ greatly improves the tensile strength of PVDF-LiTFSI, which increases from 4.9 to 8.4 MPa. In addition, the maximum strain of 1LBH-CPE exceeds 300%. This enhancement in mechanical stability may be ascribed to the ability of $Li_2B_{12}H_{12}$ to enhance the dispersion of inorganic particles in the PVDF-LiTFSI polymer matrix.

The excellent $Li^+$ conduction property and electrochemical and mechanical stability of 1LBH-CPE imply that the material exhibits superior electrode compatibility. Symmetric Li cells were assembled and tested at various current densities and temperatures to evaluate the Li anode compatibilities of PVDF-

  

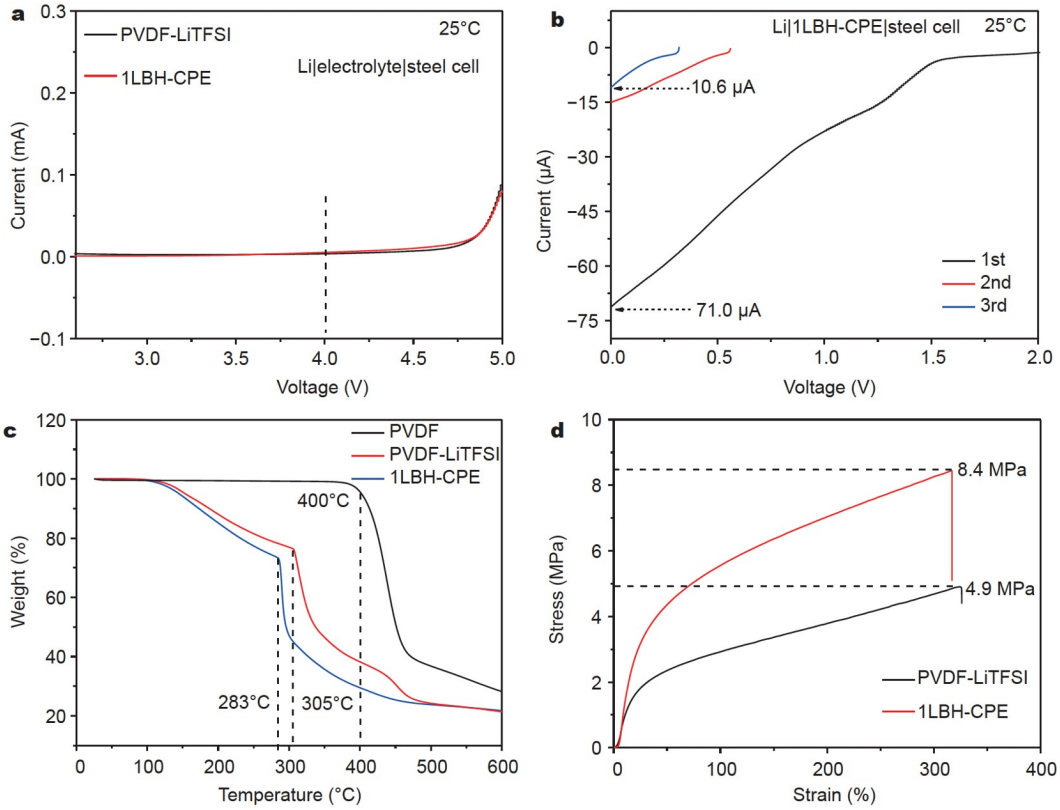


**Figure 4** (a) LSV curves of Li||steel cells based on PVDF-LiTFSI and 1LBH-CPE. (b) Repeated LSV curves of Li|1LBH-CPE|steel from the OCV to 0 V. (c) TGA curves of PVDF, PVDF-LiTFSI, and 1LBH-CPE. (d) Stress-strain curves of PVDF-LiTFSI and 1LBH-CPE.

LiTFSI and 1LBH-CPE. Fig. 5a shows the GCD curves of symmetric PVDF-LiTFSI and 1LBH-CPE-based Li cells measured at 0.2 mA $cm^{-2}$ and 25°C. The Li|PVDF-LiTFSI|Li cell can only be stably cycled for less than 70 h, beyond which its polarization voltage begins to increase sharply from 200 mV to over 1.5 V until the cell eventually short-circuits. By comparison, the 1LBH-CPE-based Li cell can be stably cycled for over 1200 h under identical conditions without apparent polarization voltage fluctuation. The polarization voltage of the cell in the initial 20 h of cycling is flat and ranges from 94 to 120 mV, after which it increases to 160 mV after 1000 cycles (Fig. 5b, c). The GCD curves of these symmetric Li cells at higher temperatures and current densities (Fig. S11) also demonstrate that $Li_2B_{12}H_{12}$ addition can effectively improve the Li compatibility of PVDF-LiTFSI. Specifically, the 1LBH-CPE-based Li cell shows stable cycling at up to 3 mA $cm^{-2}$ and 65°C, two times as large as that of the PVDF-LiTFSI-based Li cell. The continuous increase in the polarization voltage of PVDF-LiTFSI, which indicates poor Li compatibility, may be ascribed to the occurrence of supplementary reactions between Li and PVDF-LiTFSI and the thickening of the SEI.

$Li_2B_{12}H_{12}$ in the 1LBH-CPE-based cell can help form a highly stable LiH-containing SEI, which prevents the development of side reactions at the anode/electrolyte interface during cycling.

The cathode compatibility of 1LBH-CPE was evaluated by assessing the electrochemical performance of the Li|1LBH-CPE|$LiFePO_4$ cell at 25°C. All cells were activated prior to the measurements (Fig. S12). Fig. 6a shows the rate performances of PVDF-LiTFSI and 1LBH-CPE-based cells in the voltage range of 2.8–3.8 V. The reversible specific capacity (based on $LiFePO_4$) of the Li|1LBH-CPE|$LiFePO_4$ cell reaches 152, 149, 145, 139, 127, 115, and 90 mA h $g^{-1}$ at 0.1, 0.2, 0.5, 1, 2, 3, and 5 C, respectively, and recovers to 153 mA h $g^{-1}$ when the current density returns to 0.1 C. The rate performance of the Li|PVDF-LiTFSI|$LiFePO_4$ cell is much lower than that of the Li|1LBH-CPE|$LiFePO_4$ cell; specifically, the Li|PVDF-LiTFSI|$LiFePO_4$ cell generates a reversible specific capacity of only 42 mA h $g^{-1}$ at 5 C, which is less than half of that achieved by the Li|1LBH-CPE|$LiFePO_4$ cell under the same condition.

Long-term cycling at 1 C was performed to demonstrate the cycling stability of the PVDF-LiTFSI and 1LBH-CPE-based Li|$LiFePO_4$ cells. Fig. 6b presents the GCD curves of the Li|1LBH-CPE|$LiFePO_4$ cell at different cycles. Typical charge and discharge plateaus near 3.45 V with a voltage hysteresis of 180 mV can be observed in the first cycle, which indicates an acceptable internal resistance in the cell [52]. Moreover, the regular overlap of the GCD curves in the following cycles suggests excellent interfacial stability between the electrode and electrolyte. By comparison, the voltage hysteresis of the Li|PVDF-LiTFSI|$LiFePO_4$ cell is higher, and its interfacial stability appears to be poorer (Fig. S13). The cycling performance plots in Fig. 6c reveal that the Li|1LBH-CPE|$LiFePO_4$ cell produces an initial reversible specific capacity of 139 mA h $g^{-1}$ with a Coulombic efficiency of 98%. The reversible specific capacity of the cell remains nearly unchanged in the following cycles, with a Coulombic efficiency close to 100%, which corresponds to a capacity retention of 98% after 200 cycles. By comparison, the initial reversible specific capacity of the Li|PVDF-LiTFSI|$LiFePO_4$ cell is lower

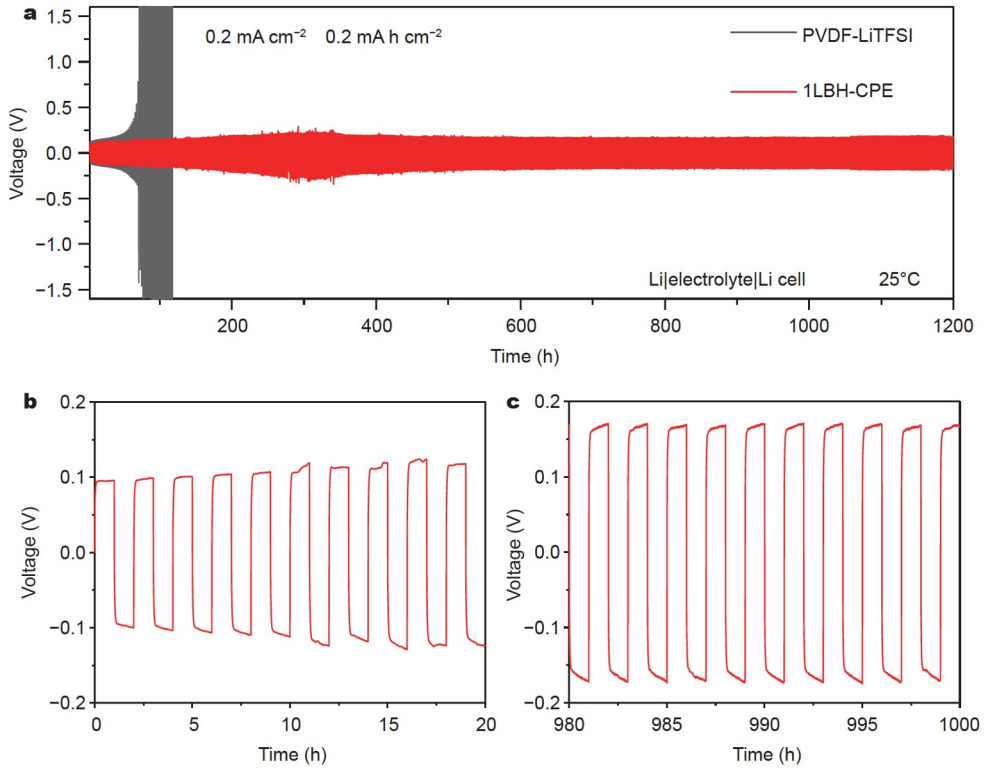


**Figure 5** (a) GCD profiles of symmetrical Li cells based on PVDF-LiTFSI and 1LBH-CPE at 0.2 mA cm$^{-2}$. Enlarged images of the GCD curves for the time periods of (b) 0–20 h and (c) 980–1000 h.

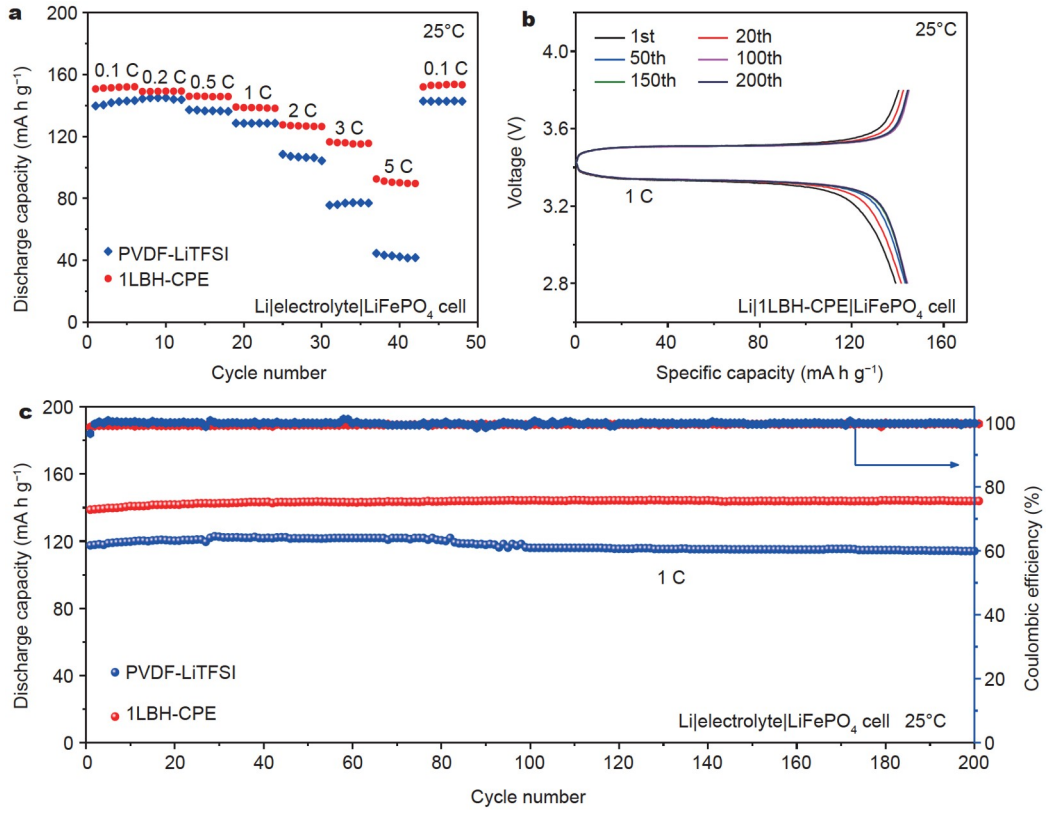


**Figure 6** (a) Rate performances of Li||$LiFePO_4$ cells based on PVDF-LiTFSI and 1LBH-CPE. (b) GCD curves of the Li|1LBH-CPE|$LiFePO_4$ cell at different cycles at 1 C. (c) Long-term cycling performances of Li||$LiFePO_4$ cells based on PVDF-LiTFSI and 1LBH-CPE at 1 C.

  

($118\ mA\ h\ g^{-1}$) and its capacity retention is only 95% after 200 cycles. The superior electrochemical performance of the Li|1LBH-CPE|$LiFePO_4$ cell can be attributed to the presence of $Li_2B_{12}H_{12}$, which improves the $Li^+$ conductivity of the reaction system by providing rapid transfer pathways and enhances the electrochemical stability of the cell by forming a protective SEI.

## CONCLUSIONS

In conclusion, flexible LBH-CPEs were successfully prepared *via* the conventional solution-casting method. Bounded NMP, which acts as a plasticizer for PVDF, is detected in the CPEs after drying. Among the LBH-CPEs fabricated, 1LBH-CPE exhibits the highest conductivity ($1.43 \times 10^{-4}\ S\ cm^{-1}$) and $Li^+$ transference number (0.34) at 25°C. The significant improvement in the $Li^+$ conduction performance of the LBH-CPEs may be attributed to the interaction between $Li_2B_{12}H_{12}$ (*via* its electron-deficient multicenter bonds) and LiTFSI, which facilitates the dissociation of LiTFSI to provide more free $Li^+$ and enhance the immobilization of $TFSI^-$ by charge exchange. The sample 1LBH-CPE demonstrates an apparent electrochemical stability window of 0–4.0 V, good thermal stability below 100°C, and tensile strength of 8.4 MPa. The anode compatibility of LBH-CPE is significantly improved by the formation of a protective SEI at the anode/electrolyte interface, which prevents the occurrence of side reactions. The Li|1LBH-CPE|Li cells present superior performance over 1200 h of cycling at a current density of $0.2\ mA\ cm^{-2}$ and temperature of 25°C. Moreover, the Li|LBH-CPE|$LiFePO_4$ cells exhibit good rate performance and excellent cycling performance, as evidenced by their generation of a reversible specific capacity of $140\ mA\ h\ g^{-1}$ at 1 C and 25°C after 200 cycles.

**Received 21 March 2021; accepted 15 June 2021; published online 19 August 2021**


1 Shi Y, Tan D, Li M, *et al.* Nanohybrid electrolytes for high-energy lithium-ion batteries: Recent advances and future challenges. Nanotechnology, 2019, 30: 302002
2 Yue L, Ma J, Zhang J, *et al.* All solid-state polymer electrolytes for high-performance lithium ion batteries. Energy Storage Mater, 2016, 5: 139–164
3 Pang Y, Pan J, Yang J, *et al.* Electrolyte/electrode interfaces in all-solid-state lithium batteries: A Review. Electrochem Energ Rev, 2021, 4: 169–193
4 Liu L, Lyu J, Mo J, *et al.* Flexible, high-voltage, ion-conducting composite membranes with 3D aramid nanofiber frameworks for stable all-solid-state lithium metal batteries. Sci China Mater, 2020, 63: 703–718
5 Huo H, Chen Y, Luo J, *et al.* Rational design of hierarchical "ceramic-in-polymer" and "polymer-in-ceramic" electrolytes for dendrite-free solid-state batteries. Adv Energy Mater, 2019, 9: 1804004
6 Meyer WH. Polymer electrolytes for lithium-ion batteries. Adv Mater, 1998, 10: 439–448
7 Choi SW, Kim JR, Jo SM, *et al.* Electrochemical and spectroscopic properties of electrospun PAN-based fibrous polymer electrolytes. J Electrochem Soc, 2005, 152: A989
8 Achari VB, Reddy TJR, Sharma AK, *et al.* Electrical, optical, and structural characterization of polymer blend (PVC/PMMA) electrolyte films. Ionics, 2007, 13: 349–354
9 Yao P, Zhu B, Zhai H, *et al.* PVDF/palygorskite nanowire composite electrolyte for 4 V rechargeable lithium batteries with high energy density. Nano Lett, 2018, 18: 6113–6120
10 Dirican M, Yan C, Zhu P, *et al.* Composite solid electrolytes for all-solid-state lithium batteries. Mater Sci Eng-R-Rep, 2019, 136: 27–46
11 Guo Q, Han Y, Wang H, *et al.* New class of LAGP-based solid polymer composite electrolyte for efficient and safe solid-state lithium batteries. ACS Appl Mater Interfaces, 2017, 9: 41837–41844
12 Guo X, Peng W, Wu Y, *et al.* $Al_4B_2O_9$ nanorods-modified solid polymer electrolytes with decent integrated performance. Sci China Mater, 2020, 64: 296–306
13 Polu AR, Rhee HW. Effect of $TiO_2$ nanoparticles on structural, thermal, mechanical and ionic conductivity studies of $PEO_{12}$-LiTDI solid polymer electrolyte. J Industrial Eng Chem, 2016, 37: 347–353
14 Pitawala HMJC, Dissanayake MAKL, Seneviratne VA, *et al.* Effect of plasticizers (EC or PC) on the ionic conductivity and thermal properties of the $(PEO)_9LiTF:Al_2O_3$ nanocomposite polymer electrolyte system. J Solid State Electrochem, 2008, 12: 783–789
15 Zhu LJ, Zhu LP, Zhang PB, *et al.* Surface zwitterionicalization of poly (vinylidene fluoride) membranes from the entrapped reactive core-shell silica nanoparticles. J Colloid Interface Sci, 2016, 468: 110–119
16 Li B, Su Q, Yu L, *et al.* $Li_{0.35}La_{0.55}TiO_3$ nanofibers enhanced poly(vinylidene fluoride)-based composite polymer electrolytes for all-solid-state batteries. ACS Appl Mater Interfaces, 2019, 11: 42206–42213
17 Zhao Y, Yan J, Cai W, *et al.* Elastic and well-aligned ceramic LLZO nanofiber based electrolytes for solid-state lithium batteries. Energy Storage Mater, 2019, 23: 306–313
18 Shi X, Ma N, Wu Y, *et al.* Fabrication and electrochemical properties of LATP/PVDF composite electrolytes for rechargeable lithium-ion battery. Solid State Ion, 2018, 325: 112–119
19 Chen S, Zhao Y, Yang J, *et al.* Hybrid solid electrolytes with excellent electrochemical properties and their applications in all-solid-state cells. Ionics, 2016, 23: 2603–2611
20 Wu N, Chien PH, Li Y, *et al.* Fast $Li^+$ conduction mechanism and interfacial chemistry of a NASICON/polymer composite electrolyte. J Am Chem Soc, 2020, 142: 2497–2505
21 Zhang X, Liu T, Zhang S, *et al.* Synergistic coupling between $Li_{6.75}La_3Zr_{1.75}Ta_{0.25}O_{12}$ and poly(vinylidene fluoride) induces high ionic conductivity, mechanical strength, and thermal stability of solid composite electrolytes. J Am Chem Soc, 2017, 139: 13779–13785
22 Yang L, Wang Z, Feng Y, *et al.* Flexible composite solid electrolyte facilitating highly stable "soft contacting" Li-electrolyte interface for solid state lithium-ion batteries. Adv Energy Mater, 2017, 7: 1701437
23 Pan K, Zhang L, Qian W, *et al.* A flexible ceramic/polymer hybrid solid electrolyte for solid-state lithium metal batteries. Adv Mater, 2020, 32: 2000399
24 Pang Y, Wang X, Shi X, *et al.* Solid-state prelithiation enables high-performance Li-Al-H anode for solid-state batteries. Adv Energy Mater, 2020, 10: 1902795
25 Paskevicius M, Jepsen LH, Schouwink P, *et al.* Metal borohydrides and derivatives—Synthesis, structure and properties. Chem Soc Rev, 2017, 46: 1565–1634
26 Lu Z, Ciucci F. Metal borohydrides as electrolytes for solid-state Li, Na, Mg, and Ca batteries: A first-principles study. Chem Mater, 2017, 29: 9308–9319
27 Cuan J, Zhou Y, Zhou T, *et al.* Borohydride-scaffolded Li/Na/Mg fast ionic conductors for promising solid-state electrolytes. Adv Mater, 2019, 31: 1803533
28 Lu F, Pang Y, Zhu M, *et al.* A high-performance Li-B-H electrolyte for all-solid-state Li batteries. Adv Funct Mater, 2019, 29: 1809219
29 Teprovich JA, Colón-Mercado H, Washington II AL, *et al.* Bi-functional $Li_2B_{12}H_{12}$ for energy storage and conversion applications: Solid-state electrolyte and luminescent down-conversion dye. J Mater Chem A, 2015, 3: 22853–22859
30 Shi X, Pang Y, Wang B, *et al. In situ* forming LiF nanodecorated electrolyte/electrode interfaces for stable all-solid-state batteries. Mater Today Nano, 2020, 10: 100079
31 Li S, Ju X, Wan C. First-principles calculations of structural, elastic and electronic properties of $Li_2B_{12}H_{12}$. J Alloys Compd, 2014, 593: 169–175
32 Pitt MP, Paskevicius M, Brown DH, *et al.* Thermal stability of $Li_2B_{12}H_{12}$ and its role in the decomposition of $LiBH_4$. J Am Chem Soc, 2013, 135: 6930–6941
33 Kresse G, Furthmüller J. Efficient iterative schemes for *ab initio* total-energy calculations using a plane-wave basis set. Phys Rev B, 1996, 54:


  

11169–11186
34 Vanderbilt D. Soft self-consistent pseudopotentials in a generalized eigenvalue formalism. Phys Rev B, 1990, 41: 7892–7895
35 Perdew JP, Zunger A. Self-interaction correction to density-functional approximations for many-electron systems. Phys Rev B, 1981, 23: 5048–5079
36 Perdew JP, Burke K, Ernzerhof M. Generalized gradient approximation made simple. Phys Rev Lett, 1996, 77: 3865–3868
37 Dion M, Rydberg H, Schröder E, *et al.* Van der Waals density functional for general geometries. Phys Rev Lett, 2004, 92: 246401
38 Sun Y, Zhan X, Hu J, *et al.* Improving ionic conductivity with bimodal-sized $Li_7La_3Zr_2O_{12}$ fillers for composite polymer electrolytes. ACS Appl Mater Interfaces, 2019, 11: 12467–12475
39 Muetterties EL, Merrifield RE, Miller HC, *et al.* Chemistry of boranes. III. 1 the infrared and Raman spectra of $B_{12}H_{12}^-$ and related anions. J Am Chem Soc, 1962, 84: 2506–2508
40 Bag S, Zhou C, Kim PJ, *et al.* LiF modified stable flexible PVDF-garnet hybrid electrolyte for high performance all-solid-state Li-S batteries. Energy Storage Mater, 2020, 24: 198–207
41 Zhao Y, Wu C, Peng G, *et al.* A new solid polymer electrolyte incorporating $Li_{10}GeP_2S_{12}$ into a polyethylene oxide matrix for all-solid-state lithium batteries. J Power Sources, 2016, 301: 47–53
42 Li Y, Arnold W, Thapa A, *et al.* Stable and flexible sulfide composite electrolyte for high-performance solid-state lithium batteries. ACS Appl Mater Interfaces, 2020, 12: 42653–42659
43 Bruce P. Conductivity and transference number measurements on polymer electrolytes. Solid State Ion, 1988, 28-30: 918–922
44 Bruce PG, Vincent CA. Steady state current flow in solid binary electrolyte cells. J Electroanal Chem Interfacial Electrochem, 1987, 225: 1–17
45 Ohba N, Miwa K, Aoki M, *et al.* First-principles study on the stability of intermediate compounds of $LiBH_4$. Phys Rev B, 2006, 74: 075110
46 Verdal N, Her JH, Stavila V, *et al.* Complex high-temperature phase transitions in $Li_2B_{12}H_{12}$ and $Na_2B_{12}H_{12}$. J Solid State Chem, 2014, 212: 81–91
47 Chen H, Adekoya D, Hencz L, *et al.* Stable seamless interfaces and rapid ionic conductivity of Ca-$CeO_2$/LiTFSI/PEO composite electrolyte for high-rate and high-voltage all-solid-state battery. Adv Energy Mater, 2020, 10: 2000049
48 Xu H, Chien PH, Shi J, *et al.* High-performance all-solid-state batteries enabled by salt bonding to perovskite in poly(ethylene oxide). Proc Natl Acad Sci USA, 2019, 116: 18815–18821
49 Zhu M, Pang Y, Lu F, *et al. In situ* formed Li-B-H complex with high Li-ion conductivity as a potential solid electrolyte for Li batteries. ACS Appl Mater Interfaces, 2019, 11: 14136–14141
50 Callegari D, Bonizzoni S, Berbenni V, *et al.* Is it possible to obtain solvent-free, $Li^+$-conducting solid electrolytes based on pure PVDF? Comment on "self-suppression of lithium dendrite in all-solid-state lithium metal batteries with poly(vinylidene difluoride)-based solid electrolytes". Adv Mater, 2020, 32: 1907375
51 Zhang X, Wang S, Xue C, *et al.* Response to comment on "self-suppression of lithium dendrite in all-solid-state lithium metal batteries with poly(vinylidene difluoride)-based solid electrolytes". Adv Mater, 2020, 32: 2000026
52 Lin Y, Gao MX, Zhu D, *et al.* Effects of carbon coating and iron phosphides on the electrochemical properties of $LiFePO_4$/C. J Power Sources, 2008, 184: 444–448

**Acknowledgements** This work was supported by the National Natural Science Foundation of China (51971146 and 51971147), the Major Program for the Scientific Research Innovation Plan of Shanghai Education Commission (2019-01-07-00-07-E00015), Shanghai Outstanding Academic Leaders Plan, Guangxi Key Laboratory of Information Materials (Guilin University of Electronic Technology, 201017-K), Shanghai Rising-Star Program (20QA1407100), and the General Program of Natural Science Foundation of Shanghai (20ZR1438400).

**Author contributions** Pang Y and Zheng S proposed the idea; Bao K conducted the experiments; Bao K and Fang F performed the data analysis; Bao K and Pang Y wrote the paper with support from Yang J and Zheng S; Pang Y and Sun D contributed to the theoretical analysis. All authors contributed to the general discussion.

**Conflict of interest** The authors declare that they have no conflict of interest.

**Supplementary information** Supporting data are available in the online version of the paper.

**Kepan Bao** received his BS degree from the School of Energy and Environmental Engineering at the University of Science and Technology Beijing in 2018. Currently, he is an MS student at the School of Materials Science and Engineering, University of Shanghai for Science and Technology. His research focuses on composite solid electrolytes for solid-state batteries.

**Yuepeng Pang** received his PhD degree from the Department of Materials Science and Engineering at Zhejiang University in 2014. He is currently an associate professor at the School of Materials Science and Engineering, University of Shanghai for Science and Technology. His current research mainly focuses on hydride materials for solid-state batteries.

**Fang Fang** received his PhD degree from the Department of Materials Science at Fudan University in 2009. He is currently a professor at the Department of Materials Science, Fudan University. His current research interests focus on high-performance hydrogen storage materials and key materials for solid-state batteries.

**Shiyou Zheng** received his BS, MS, and PhD degrees from Sichuan University, Zhejiang University, and Fudan University, respectively. He became a visiting researcher at the National Institute of Standards and Technology and the University of Maryland and is currently a professor at the University of Shanghai for Science and Technology. His research interests include new energy materials for batteries, supercapacitors, and hydrogen storage. He was selected as a "Young and Middle-aged Experts with Outstanding Experts" by the New Century Talents Project in 2019.

  

# 闭式硼氢化锂基聚合物复合电解质实现25°C下固态锂电池的高稳定循环

保克晔[1], 庞越鹏[1*], 杨俊和[1], 孙大林[2], 方方[2*], 郑时有[1*]

**摘要** 合理的成分设计是固态锂电池用高性能复合电解质开发的重要策略. 本文将闭式硼氢化锂$Li_2B_{12}H_{12}$引入到含非游离态*N*-甲基吡咯烷酮塑化剂的聚偏二氟乙烯-双三氟甲基磺酰亚胺锂(PVDF-LiTFSI)中, 制成新型复合聚合物电解质. 该电解质在25°C时具有$1.43 \times 10^{-4}$ S cm$^{-1}$的电导率和0.34的锂离子迁移数, 显示出优异的导锂性能. 密度泛函理论计算表明, 具有缺电子多中心键的$Li_2B_{12}H_{12}$可以促进LiTFSI的解离和$TFSI^-$的固定, 是锂离子导电性能改善的主要原因. 此外, 该电解质还具有出色的电化学、热力学和机械稳定性. $Li_2B_{12}H_{12}$的添加有助于在负极/电解质界面形成保护性中间相, 阻止副反应的进一步发生. 由于上述优势, 该电解质具有很高的电极兼容性, 如锂对称电池可以在0.2 mA cm$^{-2}$下稳定循环1200多个小时, Li||$LiFePO_4$电池在1 C和25°C的条件下经200个循环仍可以保持140 mA h g$^{-1}$的可逆比容量, 容量保持率为98%.

  